Polarization-insensitive reverse-ridge AlGaAs waveguide for the mid-infrared supercontinuum generation

Luqi Zhang [a], Jinhui Yuan [a,b,*], Yujun Cheng [a], Chao Mei [b], Jintao Lai [a], Xian Zhou [b], Qiang Wu [c,d], Binbin Yan [a], Kuiru Wang [a,*], Chongxiu Yu [a], Xinzhu Sang [a]

[a]*State Key Laboratory of Information Photonics and Optical Communications, Beijing University of Posts and Telecommunications, Beijing 100876, China*
[b]*Research Center for Convergence Networks and Ubiquitous Services, University of Science & Technology Beijing (USTB), Beijing 100083, China*
[c]*Department of Physics and Electrical Engineering, Northumbria University, Newcastle upon Tyne, NE1 8ST, United Kingdom*
[d]*Key Laboratory of Nondestructive Test (Ministry of Education), Nanchang Hangkong University, Nanchang 330063, China*
[*]Corresponding authors: yuanjinhui81@bupt.edu.cn; krwang@bupt.edu.cn

Abstract: In this paper, a polarization-insensitive reverse-ridge AlGaAs waveguide is designed for the supercontinuum generation. In the considered wavelength range from 3.4 to 8 μm, the dispersion profiles, nonlinear coefficients, and effective mode field areas for the quasi-TE and quasi-TM modes coincide well. The simulation results show that when pump pulse with wavelength of 4.2 μm, peak power of 4.8 kW, and width of 90 fs is launched into the anomalous dispersion region of the quasi-TE and quasi-TM modes of the 3.4-mm-long waveguide, the two generated SCs overlap well. For the quasi-TE and quasi-TM modes, the SCs generated extend from 2.17 to 8.53 μm and 2.23 to 8.61 μm, respectively, spanning more than 1.95 octaves. The proposed reverse-ridge AlGaAs waveguide structure is expected to provide a possible solution for alleviating the undesired polarization effect related to the nonlinear dynamics.

Keywords: Reverse-ridge AlGaAs waveguide, Polarization insensitivity, Supercontinuum generation

1. Introduction

Mid-infrared supercontinuum (SC) generation is of great interest for its applications in spectroscopy [1-5], optical coherence tomography [6-8], biomedical imaging [9], ladar [10, 11], gas sensing [12-14], etc. As well known, the interaction of dispersive and nonlinear effects, which includes self-phase modulation (SPM), cross-phase modulation (XPM), four-wave mixing (FWM), stimulated Raman scattering (SRS), soliton fission (SF), contributes to the SC generation [15-18].

In recent years, lots of investigations on the mid-infrared SC generations in optical waveguides have been reported. Yuan et al. numerically generated the coherent and multi-octaves SC spanning from 1.96 to 12 μm in a suspended Ge-membrane ridge waveguide [19]. Saini et al. investigated the mid-infrared SC generation in the rib As_2Se_3 waveguides with different core shapes [20]. Sinobad et al. demonstrated the SC generation in the wavelength range from 2.8 to 5.7 μm in the SiGe waveguide with an all-normal dispersion profile [21]. Lu et al. reported the SC generation at the ultraviolet to mid-infrared spectral region in the single-crystalline AlN waveguide [22]. Saini et al. generated the near-infrared to mid-infrared SC in a tellurium-oxide coated silicon-nitride waveguide through pumping in the normal dispersion region [23]. Karim et al. utilized a suspended core channel As_2Se_3 waveguide for the SC generation covering from 1.5 to 15 μm [24].

AlGaAs is the alloy of AlAs and GaAs. The refractive index of AlGaAs can be easily adjusted by changing the alloy composition [25]. Therefore, the refractive index difference between the waveguide core and substrate and the dispersion characteristic can be flexibly changed. In addition, its large transparency window (more than 15 μm [26], more than twice that of Si) and strong Kerr nonlinear index (on the order of 10^{-17} m^2/W [27], an order of magnitude larger than that of Si [28]) make it suitable for the mid-infrared SC generation. Mei designed the AlGaAs strip waveguides to generate the broadband SC, spanning from 2 to 15.9 μm [29]. Chiles et al. utilized a suspended AlGaAs waveguide to generate the second-harmonic and broadband SC covering from 2.3 to 6.5 μm when pump wavelength was located at 3060 nm [30]. Kuyken et al. experimentally demonstrated an octave-spanning SC generation in the wavelength range from 1055 to 2155 nm in an AlGaAs waveguide [27]. With picojoule-level pulse energy, May et al. experimentally obtained a SC covering ~ 544 nm at the level of -25 dB in AlGaAs-on-insulator waveguides [31].

In recent years, there are some investigations on the polarization insensitivity of the waveguide-based modulator and grating. Tabti et al. demonstrated a polarization-insensitive sampled Bragg grating by exploiting the birefringence compensation in Si_3N_4 waveguide [32], where the transmission spectra for both the quasi-transverse electric (TE) and quasi-transverse magnetic (TM) modes overlapped over a spectral range of 40 nm. Chen et al. proposed a polarization-insensitive graphene modulator, which was polarization-independent for the TE and TM modes [33]. Zhou et al. reported a polarization-insensitive graphene-based optical modulator integrated in a chalcogenide glass waveguide [34], where the absorption coefficient variation was almost identical in the wavelength range of 2-2.4 μm for the TE and TM modes. However, there is still no report on the polarization-insensitive waveguide for the SC generation. For the SC generation, the nonlinear process is always very sensitive to the polarization state of the pump light because the dispersion and nonlinear characteristics of the quasi-TE and quasi-TM modes of the waveguides are different. Thus, the polarization state of the pump light needs to be controlled by employing the polarization controller [35-38]. At this time, the complexity of the experimental system is increased, and the undesired polarization effect has an adverse influence on the energy conversion caused by the nonlinear effects. At present, the polarization-dependent problem of the pump light could be effectively solved by reasonably designing the waveguide structure.

In this paper, a polarization-insensitive reverse-ridge AlGaAs waveguide is proposed to generate the mid-infrared SCs. In the design, the influences of the geometrical parameters of the waveguide on the dispersion characteristic are analyzed to optimize the waveguide structure. In addition, the impacts of the pump pulse parameters and waveguide length on the SC generations are also investigated. With the designed 3.4-mm-long waveguide, for the quasi-TE and quasi-TM modes, highly coherent and octave-spanning mid-infrared SCs are generated, spanning from 2.17 to 8.53 μm and 2.23 to 8.61 μm, respectively, when pump pulse with wavelength of 4.2 μm, peak power of 4.8 kW, and width of 90 fs is used.

2. Theoretical model

The process of the SC generation in the optical waveguides can be described by the modified generalized nonlinear Schrödinger equation (GNLSE) as following [15]

$$\frac{\partial A}{\partial z}+\frac{\alpha}{2}A-\sum_{m\geq 0}\frac{i^{m+1}\beta_m(\omega)}{m!}\frac{\partial^m A}{\partial t^m}=i\left(\gamma(\omega_0)+i\gamma_1(\omega_0)\frac{\partial}{\partial t}\right)\times\left(A(z,t)\int_0^{+\infty}R(t')\left|A(z,t-t')\right|^2dt'\right), \quad (1)$$

where $A(z, t)$ stands for the slowly varying envelope of the electric field, and the m-th order dispersion coefficient calculated from the Taylor expansion of the propagation constant is represented by $\beta_m(\omega)$. The last term on the right side of Eq. (1) is the instantaneous third-order nonlinear effect, which includes the SPM, self-steepening, and delayed Raman response $R(t)$. The nonlinear coefficient at central frequency ω_0 is expressed as $\gamma(\omega_0)$. And the first-order derivative of $\gamma(\omega)$ at ω_0 is indicated by $\gamma_1(\omega_0)$. The relationship between $\gamma(\omega)$ and $\gamma_1(\omega_0)$ can be represented by [15]

$$\frac{\gamma_1(\omega_0)}{\gamma(\omega_0)} = \frac{1}{\omega_0} + \left(\frac{1}{n_2(\omega)}\left(\frac{dn_2(\omega)}{d\omega}\right)\right)_{\omega=\omega_0} - \left(\frac{1}{A_{\text{eff}}(\omega)}\left(\frac{dA_{\text{eff}}(\omega)}{d\omega}\right)\right)_{\omega=\omega_0}, \quad (2)$$

where n_2 and A_{eff} stand for the nonlinear refractive index and effective mode field area, respectively. In the simulation, $n_2 = 1\times10^{-17}\text{m}^2/\text{W}$ [39]. And the Raman response function can be described as [15]

$$R(t) = (1-f_R)\delta(t) + f_R\frac{\tau_1^2+\tau_2^2}{\tau_1\tau_2^2}\exp\left(-\frac{t}{\tau_2}\right)\sin\left(\frac{t}{\tau_1}\right), \quad (3)$$

where f_R stands for the fractional contribution of the Raman response. The Raman period τ_1 is 18.72 fs, and damping time of vibrations τ_2 is 0.75 ps [40]. The coherence of the generated SC is one of the important parameters to measure the stability of the SC. And the degree of the first-order coherence $g_{12}^{(1)}$ of the SC can be described as [41]

$$g_{12}^{(1)}(\lambda) = \frac{\left\langle A_1^*(\lambda)A_2(\lambda)\right\rangle}{\sqrt{\left\langle|A_1(\lambda)|^2\right\rangle\left\langle|A_2(\lambda)|^2\right\rangle}}, \quad (4)$$

where $A(\lambda)$ represents the amplitude of the SC in the frequency domain. The expressions in the angle bracket indicate the independent certain pairs of the SC with random input noise. The 100 independent simulations will be carried out and the average value of each pair of the output fields will be calculated in this work. And the noise is described as [42]

$$n = \eta\hat{N}\exp\left(i2\pi\hat{U}\right), \quad (5)$$

where η stands for the amplitude coefficient of the noise relative to the input pulse. And $\hat{N}$ obeys the standard normal distribution while $\hat{U}$ obeys the uniform distribution.

3. Waveguide design and characteristics

Fig. 1(a) shows the three-dimensional structure of the designed reverse-ridge AlGaAs waveguide. The $Al_{0.18}Ga_{0.82}As$ layer, where the ratio of AlAs and GaAs is 0.18 to 0.82, is embedded in the $Al_{0.8}Ga_{0.2}As$ substrate, which enhances the mode field confinement. The width of the $Al_{0.18}Ga_{0.82}As$ ridge core is W. The depth of the part embedded in the substrate is H_d, and the protruding part is represented by H_u. Fig. 1(b) shows the mode field distributions of the quasi-TE and quasi-TM modes calculated at wavelengths 3.5, 5, 6.5, and 8 μm when W, H_u, and H_d are chosen as 7, 3.52, and 3.26 μm, respectively. For both the quasi-TE and quasi-TM modes, most of the mode field energy is confined in the ridge core region of the waveguide.

The group-velocity dispersion coefficient D of the guided mode can be represented by [15]

$$D = -\left(\frac{\lambda}{c}\right)\cdot\left(\frac{\partial^2 n_{\text{neff}}}{\partial\lambda^2}\right), \quad (6)$$

where λ, c, and n_{eff} stand for the wavelength, speed of light in vacuum, and effective refractive index of the guided mode, respectively.

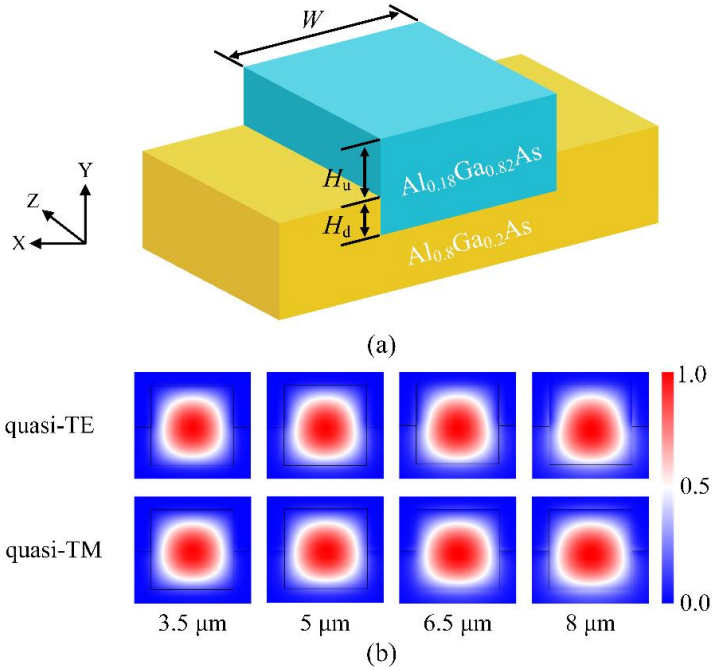

Fig. 1. (a) The three-dimensional structure of the proposed reverse-ridge AlGaAs waveguide. (b) The mode field distributions of the quasi-TE and quasi-TM modes calculated at wavelengths 3.5, 5, 6.5, and 8 μm, respectively.

The dispersion characteristics of the proposed waveguide with different geometrical parameters can be calculated by the full-vector finite element method. Fig. 2(a) shows the dispersion curves calculated for the quasi-TE and quasi-TM modes as functions of wavelength when H_u and H_d remain unchanged and W increases from 5, to 6, to 7, and to 8 μm, respectively. From Fig. 2(a), when W is less than 7 μm, the dispersion curves for the quasi-TE mode are always above those of the quasi-TM mode. As W increases, the dispersion curves of the quasi-TE and quasi-TM modes are getting closer to each other, and the zero-dispersion wavelengths (ZDWs) are gradually red-shifted. When W is larger than 7 μm, the curves for the quasi-TE mode moves down to the bottom. As shown in Fig. 2(b), with the increase of H_d, the two curves move towards the normal dispersion region, and the ZDWs are red-shifted. Owing to the larger movement of the dispersion curve for the quasi-TM mode, the two dispersion curves first get close to each other and then move away from each other. When H_d is equal to 3.26 μm, the two dispersion curves almost coincide. Figs. 2(c) and 2(d) show the influence of H_u on the dispersion characteristic and the detailed dispersion profiles of Fig. 2(c) in the wavelength range from 3.7 to 4.4 μm. The influence of H_u on the dispersion characteristic is similar to that of H_d, but the dispersion curves of the quasi-TE mode change less. For W, H_u, and H_d, the dispersion characteristic is very sensitive to W, and H_d and H_u have less influence. To obtain a polarization-insensitive waveguide, the optimized geometrical parameters are chosen as following: W=7 μm, H_u=3.52 μm, and H_d =3.26 μm.

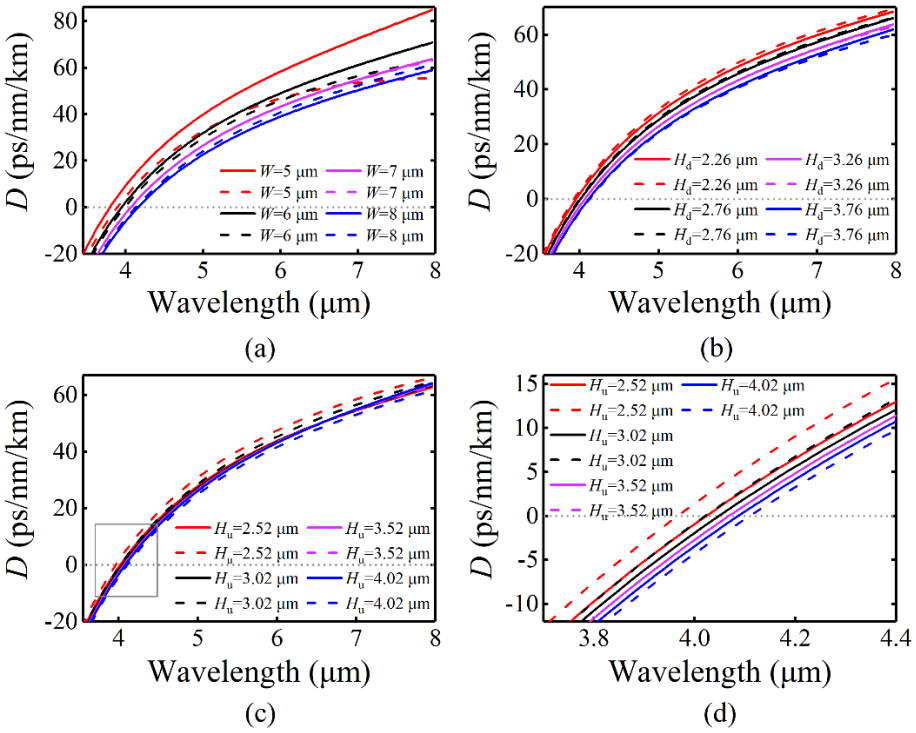

Fig. 2. (a) The dispersion curves for the quasi-TE and quasi-TM modes calculated as functions of wavelength when (a) W, (b) H_d, and (c) H_u are changed, respectively. The dispersions curves for the quasi-TE and quasi-TM modes are represented by the solid and dash curves, respectively. (d) The detailed dispersion profiles in the wavelength range from 3.7 to 4.4 μm of (c).

When W=7 μm, H_u=3.52 μm, and H_d =3.26 μm, the dispersion coefficient D, nonlinear coefficient γ, and effective mode field area A_{eff} for the quasi-TE and quasi-TM modes calculated as functions of wavelength are shown in Figs. 3(a) and 3(b), respectively. From Fig. 3(a), for the quasi-TE and quasi-TM modes, the two dispersion curves are very close in the considered wavelength range from 3.4 to 8 μm. And there is one ZDW at 4.07 μm. From Fig. 3(b), the corresponding γ curves of the quasi-TE and quasi-TM modes decrease monotonically with the increase of wavelength, while A_{eff} curves increase. Moreover, the two γ and A_{eff} curves are very similar. At the initial pump wavelength of 4.2 μm, for the quasi-TE mode, the value of D is 4.857 ps/nm/km, and the value of γ is 0.6067 /m/W. For the quasi-TM mode, the values of D and γ are 4.859 ps/nm/km and 0.6057 /m/W, respectively. Thus, the polarization-insensitive reverse-ridge AlGaAs waveguide is obtained, which is beneficial to the similar SC generations for the quasi-TE and quasi-TM modes.

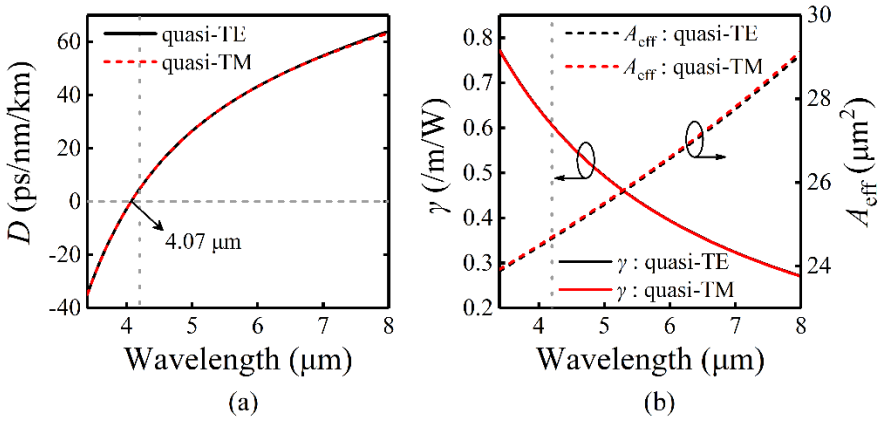

Fig. 3. (a) The chromatic dispersion curves for the quasi-TE and quasi-TM modes calculated as functions of wavelength when W=7 μm, H_u=3.52 μm, and H_d =3.26 μm. (b) The nonlinear coefficient γ and effective mode field area A_{eff} for the quasi-TE and quasi-TM modes calculated as functions of wavelength.

4. Simulation results and discussion

The SC generation in the proposed reverse-ridge AlGaAs waveguide will be numerically investigated by solving Eq. (1) with the Runge-Kutta method. While pumping in the normal dispersion region of the waveguide, the generated SC usually has good coherence with a relatively narrow spectral range. In contrast, while pumping in the anomalous dispersion region, the SC can be easily extended to a considerable range. Furthermore, the coherence of the SC can be improved by appropriately selecting the pump pulse parameters. In this simulation, the pump wavelength is located in the anomalous dispersion region, where the generation of SC mainly depends on the soliton dynamics. In the following, the influences of the pump pulse parameters, including pump wavelength, peak power, and pulse width, on the SC generation will be analyzed.

A chirp-free hyperbolic secant pump pulse is launched into the proposed reverse-ridge AlGaAs waveguide. After a propagation of 3.4 mm, the spectral and temporal profiles of the generated SCs for the quasi-TE and quasi-TM modes are shown in Figs. 4(a) and 4(b), respectively, when the wavelength of the pump pulse with peak power of 4.8 kW and width of 90 fs is changed from 4.10 to 4.25 μm. Because the pump pulse is operated in the anomalous dispersion region of the waveguide, the spectral broadening is dominated by the soliton dynamics. With the increase of the pump wavelength, the dispersion length decreases due to the increase of dispersion. The enhanced dispersion effect has an important influence on the soliton fission. As shown in Fig. 4(a), the optical spectra for the quasi-TE and quasi-TM modes are gradually broadened as the pump wavelength increases. As shown in Fig. 4(b), there are beating patterns at the rising and falling edges of the pulse. The former ones correspond to the soliton at the long wavelength side while the latter ones correspond to the dispersive wave at short wavelength side. From Figs. 4(a) and 4(b), when the pump wavelength is chosen as 4.2 μm, the generated SCs for the quasi-TE and quasi-TM modes are very similar in the spectral and temporal magnitudes and fine structures.

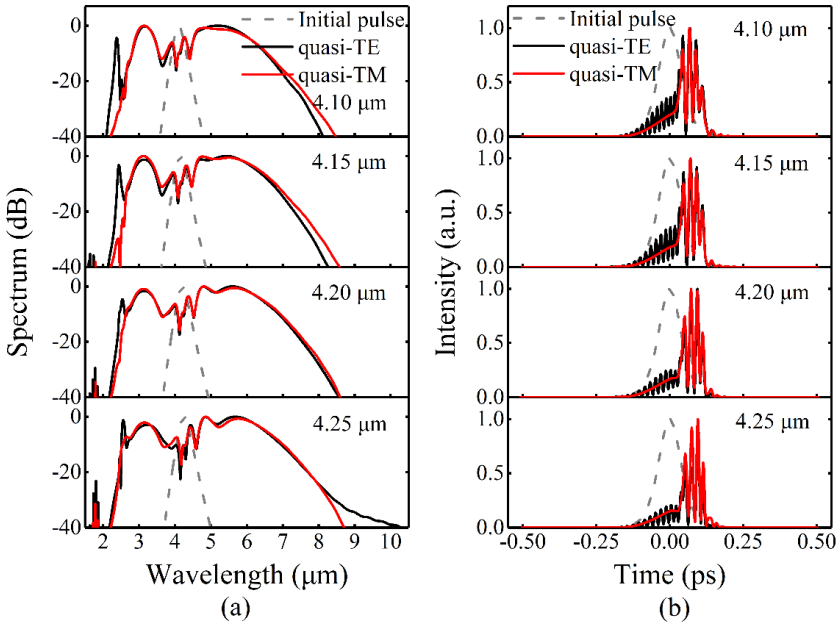

Fig. 4. The evolutions of (a) spectral and (b) temporal profiles of the pump pulse with different center wavelengths. The pump pulse and output pulses for the quasi-TE and quasi-TM modes are represented by the gray dash curves, black solid curves, and red solid curves, respectively.

Figs. 5(a) and 5(b) show the spectral and temporal profiles when the pump pulse width, wavelength, and waveguide length are chosen as 90 fs, 4.2 μm, and 3.4 mm, respectively, and the peak power of the pump pulse is changed from 1.8 to 4.8 kW. As shown in Fig. 5(a), as the peak power increases, the optical spectrum becomes asymmetric gradually due to the self-steeping effect. Compared with the red-shifted edge of the SC, the blue-shifted edge does not expand obviously. This is mainly because the dispersion slope of the waveguide is steeper at the shorter wavelength side than that at the longer wavelength side. As shown in Fig. 5(b), more beating patterns appear, which is resulted from the enhanced nonlinear effects, including the SPM and soliton fission, induced by the increased peak power. When the peak power reaches 4.8 kW, for the quasi-TE and quasi-TM modes, the generated SCs coincide well, and the spectral broadening becomes inapparent. In addition, the higher peak power will easily damage the waveguide material. Thus, the optimized peak power is chosen as 4.8 kW.

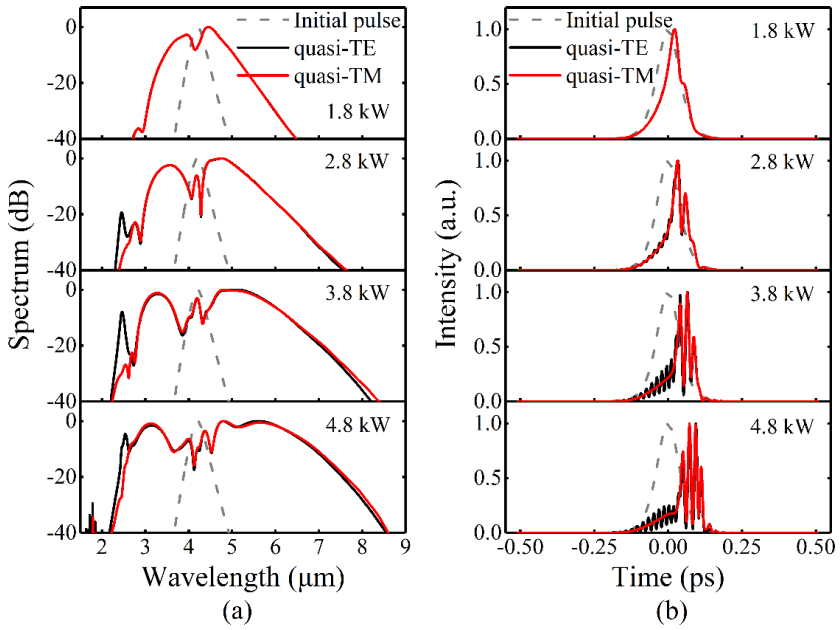

Fig. 5. The evolutions of (a) spectral and (b) temporal profiles of the pump pulse with different peak powers. The pump pulse and output pulses for the quasi-TE and quasi-TM modes are represented by the gray dash curves, black solid curves, and red solid curves, respectively.

When the pump pulses with wavelength of 4.2 μm, peak power of 4.8 kW, and width of 90, 140, 190, and 240 fs are launched into a 3.4-mm-long waveguide, the spectral and temporal profiles of the generated SCs for the quasi-TE and quasi-TM modes are shown in Figs. 6(a) and 6(b), respectively. As shown in Fig. 6(a), as the pulse width increases from 90 to 240 fs, the bandwidths of the generated SCs for the quasi-TE and quasi-TM modes gradually decrease. The main reason is considered that although the soliton order becomes larger, the soliton fission length increases, so the soliton fission does not occur due to the insufficient waveguide length. As shown in Fig. 6(b), when the pulse width increases, the temporal width becomes larger, and there are few beating patterns, which indicates that it is not conducive to generate the soliton fission. When taking the bandwidth, flatness, and coherence of the SCs into account, the suitable pulse width is chosen as 90 fs. At this time, the SC generated by the quasi-TE mode agrees well with that generated by the quasi-TM mode.

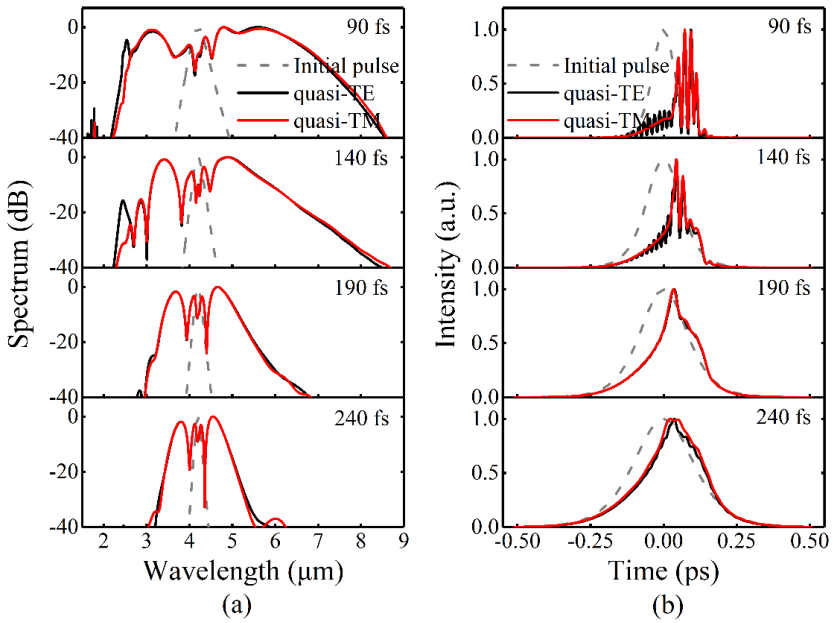

Fig. 6. The evolutions of (a) spectral and (b) temporal profiles of the pump pulse with different pulse widths. The pump pulse and output pulses for the quasi-TE and quasi-TM modes are represented by the gray dash curves, black solid curves, and red solid curves, respectively.

In the following, we will investigate the influence of the waveguide length on the SC generations. Figs. 7(a) and 7(b) show the spectral and temporal profiles for different waveguide lengths when the pump wavelength, peak power, and pulse width are chosen as 4.2 μm, 4.8 kW, and 90 fs, respectively. It can be seen from Fig. 7(a) that when the waveguide length is changed from 0.4 to 3.4 mm, the bandwidth of the generated SCs for the quasi-TE and quasi-TM modes increases gradually. As shown in Fig. 7(b), the pulse is firstly compressed due to the interaction of dispersion and SPM, and then forms the higher-order soliton. Moreover, the low and flat dispersion further compresses the pulse and broadens the optical spectrum. The spectral broadening from the anomalous to normal dispersion region provides the possibility for generating the dispersion waves [43]. When the waveguide length is larger than 3.4 mm, there is almost no increase in the spectral width due to the increased nonlinear loss. Moreover, when the higher-order soliton is completely split, the coherence of the generated SCs will be degraded due to the enhancement of the soliton disturbance. Therefore, the waveguide length of 3.4 mm is the optimized value.

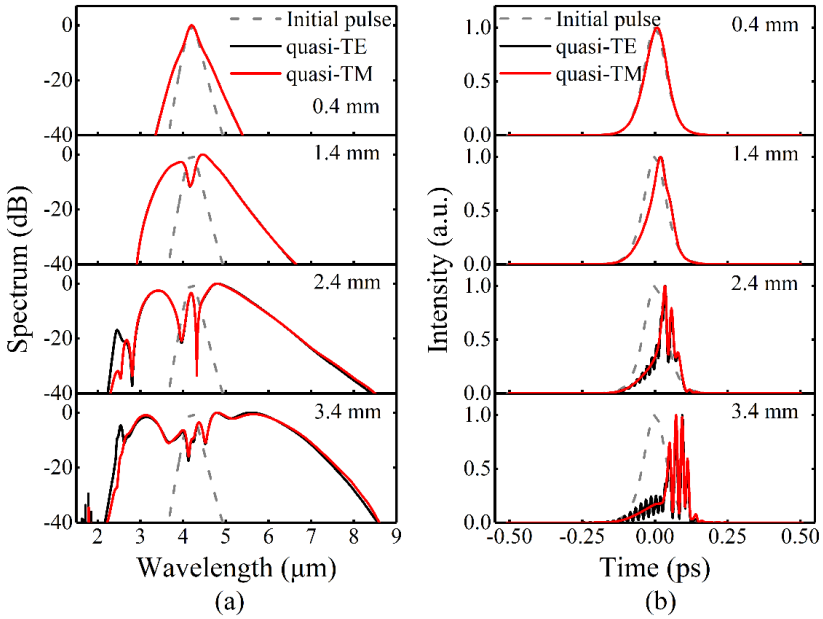

Fig. 7. The evolutions of (a) spectral and (b) temporal profiles of the pump pulse with different waveguide lengths. The pump pulse and output pulses for the quasi-TE and quasi-TM modes are represented by the gray dash curves, black solid curves, and red solid curves, respectively.

Figs. 8 and 9 show the spectral and temporal evolutions for the quasi-TE and quasi-TM modes, respectively, when the pump pulse with wavelength of 4.2 μm, peak power of 4.8 kW, and pulse width of 90 fs is launched into a 3.4mm-long waveguide. It can be seen from Figs. 8 and 9 that the initial temporal compression and symmetrical spectral broadening are mainly caused by the SPM effect. As the propagation distance increases, the optical spectra continue to expand asymmetrically, which is dominated by the soliton fission and dispersive wave. Fig. 10 shows the calculated first-order degree coherence of the SCs with η=0.001. In the considered wavelength range, the coherences of the generated SCs are also mostly coincident and approximately equal to 1 for the quasi-TE and quasi-TM modes. At the output end of the waveguide, highly coherent SCs spanning from 2.17 to 8.53 μm for the quasi-TE mode and spanning from 2.23 to 8.61 μm for the quasi-TM mode are generated. Both of the generated SCs for the quasi-TE and quasi-TM modes cover more than 1.95 octaves at -40 dB level.

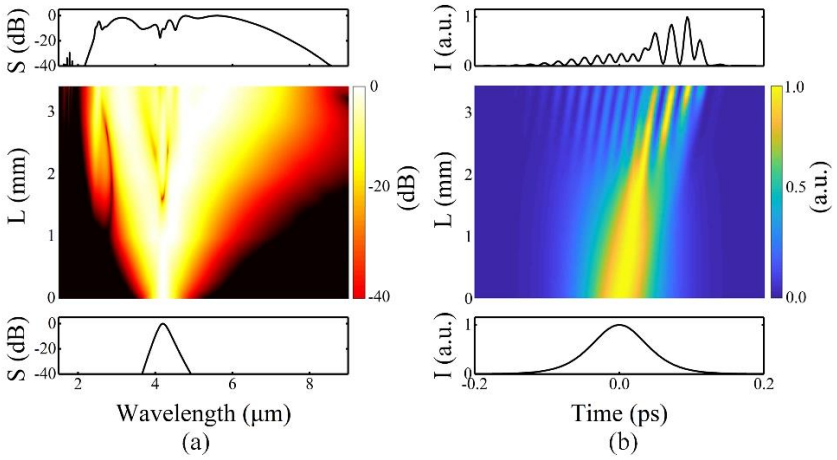

Fig. 8. (a) Spectral and (b) temporal evolutions for the quasi-TE mode along the waveguide length. The spectral and temporal profiles at the input and output ends of the waveguide are shown at the bottom and top. The spectrum is expressed as '*S*' and the intensity is expressed as '*I*'.

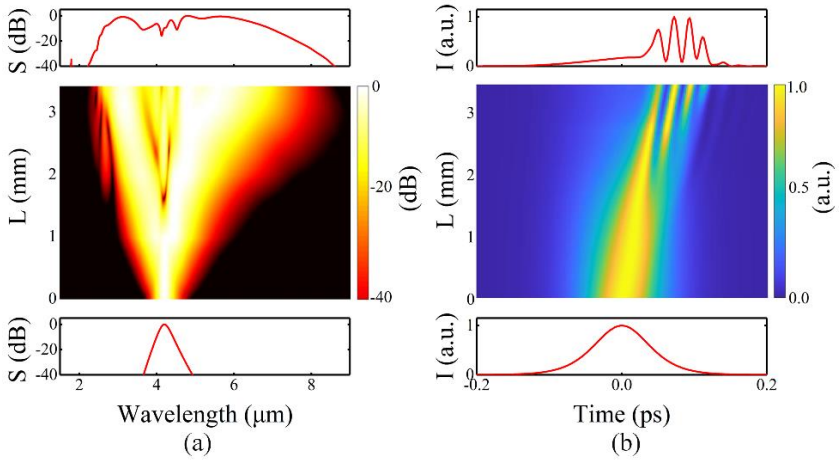

Fig. 9. (a) Spectral and (b) temporal evolutions for the quasi-TM mode along the waveguide length. The spectral and temporal profiles at the input and output ends of the waveguide are shown at the bottom and top. The spectrum is expressed as '*S*' and the intensity is expressed as '*I*'.

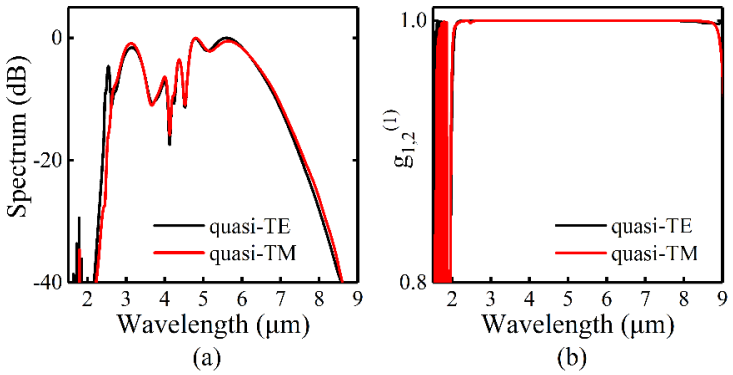

Fig. 10. (a) The generated SCs and (b) first-order degree of coherence of the SCs for the quasi-TE and quasi-TM modes calculated with η=0.001.

The reverse-strip waveguides have already been fabricated in 2019 [44]. A possible fabrication process of the proposed waveguide is shown in Figs. 11(a)-11(f). First, the $Al_{0.8}Ga_{0.2}As$ substrate is cleaned enough (Fig. 11(a)). Second, the upper surface of the substrate with N244 photoresist is covered (Fig. 11(b)). Third, the ultraviolet lithographic patterning and ICP etching are utilized to form a micro-trench (Figs. 11(c)-11(d)). Fourth, by the thermal evaporation, the $Al_{0.18}Ga_{0.82}As$ films will be grown on the substrate (Fig. 11(e)). Finally, 99.9% NMP is exploited to remove the excess, and a reverse-ridge waveguide is obtained (Fig. 11(f)).

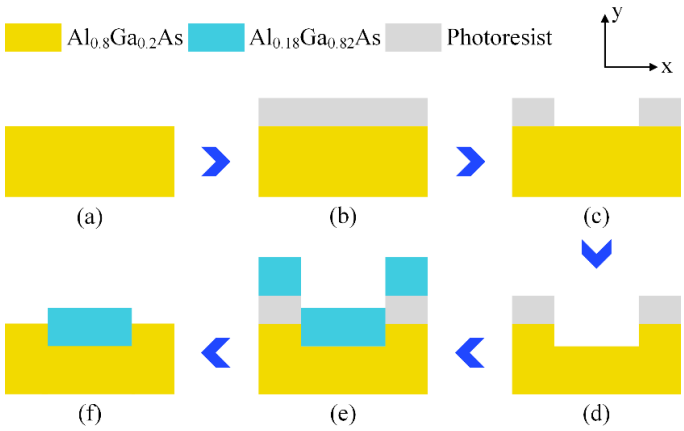

Fig. 11. A possible fabrication process flow: (a) clean of $Al_{0.8}Ga_{0.2}As$ substrate, (b) coverage of photoresist on the substrate, (c) ultraviolet exposure and development, (d) plasma etching, (e) deposition of $Al_{0.18}Ga_{0.82}As$, and (f) lifting off.

5. Conclusion

In summary, we design a polarization-insensitive reverse-ridge AlGaAs waveguide for the SC generations based on the quasi-TE and quasi-TM modes. The dispersion difference between the quasi-TE and quasi-TM modes could be reduced through exactly adjusting the geometrical parameters of the waveguide. Furthermore, by optimizing the pump pulse parameters, the generated SCs for the quasi-TE and quasi-TM modes can overlap almost completely. When the pump pulse with wavelength of 4.2 μm, peak power of 4.8 kW, and width of 90 fs is injected into the 3.4-mm-long waveguide, the -40 dB bandwidths of the generated SCs for the quasi-TE and quasi-TM modes can cover more than 1.95 octaves. It is believed that the proposed reverse-ridge AlGaAs waveguide structure provides a possible solution for alleviating the undesired polarization effect related to the nonlinear dynamics.

Acknowledgements

This work was supported by the National Natural Science Foundation of China (61875238).

References

[1] F. Lu, M. Z. Jin, M. A. Belkin, Tip-enhanced infrared nanospectroscopy via molecular expansion force detection, Nat. Photonics 8 (2014) 307–312. https://doi.org/10.1038/nphoton.2013.373.
[2] C. Amiot, A. Aalto, P. Ryczkowski, J. Toivonen, G. Genty, Cavity enhanced absorption spectroscopy in the mid-infrared using a supercontinuum source, Appl. Phys. Lett. 111 (2017) 061103. https://doi.org/10.1063/1.4985263.
[3] N. Nader, D. L. Maser, F. C. Cruz, A. Kowligy, H. Timmers, J. Chiles, C. Fredrick, D. A. Westly, S. W. Nam, R. P. Mirin, J. M. Shainline, S. Diddams, Versatile silicon-waveguide supercontinuum for coherent mid-infrared spectroscopy, Apl Photonics 3 (2018) 036102. https://doi.org/10.1063/1.4985263.
[4] J. Kilgus, K. Duswald, G. Langer, M. Brandstetter, Mid-Infrared Standoff Spectroscopy Using a Supercontinuum Laser with Compact Fabry–Pérot Filter Spectrometers, Appl. Spectrosc. 72 (2018) 634-642. https://doi.org/10.1177/0003702817746696.
[5] T. Mikkonen, C. Amiot, A. Aalto, K. Patokoski, G. Genty, J. Toivonen, Broadband cantilever-enhanced photoacoustic spectroscopy in the mid-IR using a supercontinuum, Opt. Lett. 43 (2018) 5094-5097. https://doi.org/10.1364/OL.43.005094.
[6] D. L. Marks, A. L. Oldenburg, J. J. Reynolds, S. A. Boppart, Study of an ultrahigh-numerical-aperture fiber continuum generation source for optical coherence tomography, Opt. Lett. 27 (2002) 2010-2012. https://doi.org/10.1364/OL.27.002010.
[7] I. Zorin, P. Gattinger, M. Brandstetter, B. Heise, Dual-band infrared optical coherence tomography using a single supercontinuum source, Opt. Express 28 (2020) 7858-7874. https://doi.org/10.1364/OE.386398.
[8] N. M. Israelsen, C. R. Petersen, A. Barh, D. Jain, M. Jensen, G. Hannesschläger, P. Tidemand-Lichtenberg, C. Pedersen, A. Podoleanu, O. Bang, Real-time high-resolution mid-infrared optical coherence tomography, Light-Sci. Appl. 8 (2019) 11. https://doi.org/10.1038/s41377-019-0122-5.
[9] B. J. Guo, Y. Wang, C. Peng, H. L. Zhang, G. P. Luo, H. Q. Le, C. Gmachl, D. L. Sivco, M. L. Peabody, A.Y. Cho, Laser-based mid-infrared reflectance imaging of biological tissues, Opt. Express 12 (2004) 208-219. https://doi.org/10.1364/OPEX.12.000208.
[10] R. Longshore, P. Raimondi, M. Lumpkin, Selection of detector peak wavelength for optimum infrared system performance, Infrared Phys. 16 (1976) 639–647. https://doi.org/10.1016/0020-0891(76)90100-7.
[11] J. H. Kim, M. K. Chen, C. E. Yang, J. Lee, S. Yin, K. Reichard, P. Ruffin, E. Edwards, C. Brantley, C. Luo, Middle-IR supercontinuum generations and applications, Proc. SPIE 7056, Photonic Fiber and Crystal Devices: Advances in Materials and Innovations in Device Applications II, 70560V (2008). https://doi.org/10.1117/12.793942.
[12] P. Werle, F. Slemr, K. Maurer, R. Kormann, R. Mucke, B. Janker, Near-and mid-infrared laseroptical sensors for gas analysis, Opt. Laser. Eng. 37 (2002) 101-114. https://doi.org/10.1016/S0143-8166(01)00092-6.
[13] Q. Pan, K. E. Jahromi, M. A. Abbas, A. Khodabakhsh, S. M. Cristescu, F. J. M. Harren, Towards Broadband Multi-species Trace Gas Detection Using a Mid-infrared Supercontinuum Source, 2018 Conference on Lasers and Electro-Optics (CLEO) (2018).
[14] K. E. Jahromi, Q. Pan, L. Høgstedt, S. M. M. Friis, A. Khodabakhsh, P. M. Moselund, F. J. M. Harren, Mid-infrared supercontinuum-based upconversion detection for trace gas sensing, Opt. Express 27 (2019) 24469-24480. https://doi.org/10.1364/OE.27.024469.
[15] G. P. Agrawal, Nonlinear Fiber Optics, Academic, 2013.
[16] J. M. Dudley, G. Genty, S. Coen, Supercontinuum generation in photonic crystal fiber, Rev. Mod. Phys. 78 (2006) 1135–1184. https://doi.org/10.1103/RevModPhys.78.1135.
[17] A. V. Husakou, J. Herrmann, Supercontinuum generation of higher-order solitons by fission in photonic crystal fibers, Phys. Rev. Lett. 87 (2001) 203901. https://doi.org/10.1103/PhysRevLett.87.203901.
[18] Z. L. Li, J. H. Yuan, C. Mei, F. Li, X. Zhou, B. B. Yan, Q. Wu, K. R. Wang, X. Z. Sang, K. P. Long, C. X. Yu, Multi-octave mid-infrared supercontinuum and frequency comb generation in a suspended As2Se3 ridge waveguide, Appl. Opt. 58 (2019) 8404-8410. https://doi.org/10.1364/AO.58.008404.
[19] J. H. Yuan, Z. Kang, F. Li, X. T. Zhang, X. Z. Sang, Q. Wu, B. B. Yan, K. R. Wang, X. Zhou, K. P. Zhong, G. Y. Zhou, C. X. Yu, C. Lu, H. Y. Tam, P. K. A. Wai, Mid-Infrared Octave-Spanning Supercontinuum and Frequency Comb Generation in a Suspended Germanium-Membrane Ridge Waveguide, J. Lightwave Technol. 35 (2017) 2994-3002. https://doi.org/10.1109/JLT.2017.2703644.
[20] T. S. Saini, U. K. Tiwari, R. K. Sinha, Design and Analysis of Dispersion Engineered Rib Waveguides for On-Chip Mid-Infrared Supercontinuum, J. Lightwave Technol. 36 (2018) 1993-1999. https://doi.org/10.1109/JLT.2018.2800282.
[21] M. Sinobad, A. DellaTorre, R. Armand, B. Luther-Davies, P. Ma, S. Madden, A. Mitchell, D. J. Moss, Jean-Michel Hartmann, Jean-Marc Fedeli, C. Monat, C. Grillet, Mid-infrared supercontinuum generation in silicon-germanium all-normal dispersion waveguides, Opt. Lett. 45 (2020) 5008-5011. https://doi.org/10.1364/OL.402159.
[22] J. J. Lu, X. W. Liu, A. W. Bruch, L. Zhang, J. X. Wang, J. C. Yan, H. X. Tang, Ultraviolet to mid-infrared supercontinuum generation in single-crystalline aluminum nitride waveguides, Opt. Lett. 45 (2020) 4499-4502. https://doi.org/10.1364/OL.398257.

[23] T. S. Saini, V. R. Supradeepa, Tellurium-oxide coated silicon-nitride hybrid waveguide for near-to-mid-IR supercontinuum generation: design and analysis, J. Mod. Optic. 68 (2021) 29-36. https://doi.org/10.1080/09500340.2021.1874556.
[24] M. R. Karim, N. Al Kayed, G. K. Dey, B. M. A. Rahman, Design and analysis of suspended core channel waveguide made using As2Se3 glass system for mid-infrared supercontinuum generation, J. Optics 23 (2021) 015504. https://doi.org/10.1088/2040-8986/abcfd3.
[25] G. A. Siviloglou, S. Suntsov, R. El-Ganainy, R. Iwanow, G. I. Stegeman, D. N. Christodoulides, R. Morandotti, D. Modotto, A. Locatelli, C. D. Angelis, F. Pozzi, C. R. Stanley, M. Sorel, Enhanced third-order nonlinear effects in optical AlGaAs nanowires, Opt. Express 14 (2006) 9377-9384. https://doi.org/10.1364/OE.14.009377.
[26] M. J. Weber, Hand Book of Optical Materials, CRC press, Cambridge, 2003.
[27] B. Kuyken, M. Billet, F. Leo, K. Yvind, M. H. Pu, Octave-spanning coherent supercontinuum generation in an AlGaAs-on-insulator waveguide, Opt. Lett. 45 (2020) 603-606. https://doi.org/10.1364/OL.45.000603.
[28] Z. Kang, C. Mei, L. Q. Zhang, Z. C. Zhang, J. Evans, Y. J. Cheng, K. Zhu, X. T. Zhang, D. M. Huang, Y. H. Li, J. J. He, Q. Wu, B. B. Yan, K. R. Wang, X. Zhou, K. P. Long, F. Li, Q. Li, S. K. Wang, J. H. Yuan, P. K. A. Wai, S. L. He, Advanced Progress on X (3) Nonlinearity in Chip-Scale Photonic Platforms, Prog. Electromagn. Res. 170 (2021) 17-62. https://doi.org/ 10.2528/PIER20122108.
[29] C. Mei, J. H. Yuan, Z. Kang, F. Li, X. T. Zhang, B. B. Yan, X. Z. Sang, Q. Wu, X. Zhou, K. P. Zhong, L. Wang, K. R. Wang, C. X. Yu, P. K. A. Wai, Multi-octave mid-infrared supercontinuum generation in dispersion-engineered AlGaAs-based strip waveguides, 2016 15th International Conference on Optical Communications and Networks (ICOCN) (2016). https://doi.org/10.1109/ICOCN.2016.7875675.
[30] J. Chiles, N. Nader, E. J. Stanton, D. Herman, G. Moody, J. G. Zhu, J. C. Skehan, B. Guha, A. Kowligy, J. T. Gopinath, K. Srinivasan, S. A. Diddams, I. Coddington, N. R. Newbury, J. M. Shainline, S. W. Nam, R. P. Mirin, Multifunctional integrated photonics in the mid-infrared with suspended AlGaAs on silicon, Optica 6 (2019) 1246-1254. https://doi.org/10.1364/OPTICA.6.001246.
[31] S. May, M. Clerici, M. Sorel, Supercontinuum generation in dispersion engineered AlGaAs-on-insulator waveguides, Sci. Rep. 11 (2021) 2052. https://doi.org/10.1038/s41598-021-81555-3.
[32] B. Tabti, M. Menard, Polarization insensitive sampled Bragg gratings, 2017 Photonics North (PN) (2017) 1-1. https://doi.org/10.1109/PN.2017.8090554.
[33] W. Chen, Y. Xu, Y. Gao, L. J. Ji, X. B. Wang, X. Q. Sun, D. M. Zhang, A Broadband Polarization-Insensitive Graphene Modulator Based on Dual Built-in Orthogonal Slots Plasmonic Waveguide, Appl. Sci. 11 (2021) 1897. https://doi.org/10.3390/app11041897.
[34] Y. Zhou, R. G. Lu, G. B. Wang, J. B. Lyu, M. Tan, L. M. Shen, R. Lin, Z. H. Yang, Y. Liu, Graphene-Based Polarization-Independent Mid-Infrared Electro-Absorption Modulator Integrated in a Chalcogenide Glass Waveguide, Nanoscale Res. Lett. 16 (2021) 80. https://doi.org/10.1186/s11671-021-03538-7.
[35] H. R. Guo, C. Herkommer, A. Billat, D. Grassani, C. K. Zhang, M. H. P. Pfeiffer, W. L. Weng, C. S. Brès, T. J. Kippenberg, Mid-infrared frequency comb via coherent dispersive wave generation in silicon nitride nanophotonic waveguides, Nat. Photonics 12 (2018) 330–335. https://doi.org/10.1038/s41566-018-0144-1.
[36] X. Liu, M. H. Pu, B. B. Zhou, C. J. Krückel, A. Fülöp, V. Torres-Company, M. Bache, Octave-spanning supercontinuum generation in a silicon-rich nitride waveguide, Opt. Lett. 41 (2016) 2719-2722. https://doi.org/10.1364/OL.41.002719.
[37] M. Sinobad, C. Monat, B. Luther-davies, P. Ma, S. Madden, D. J. Moss, A. Mitchell, D. Allioux, R. Orobtchouk, S. Boutami, J. M. Hartmann, J. M. Fedeli, C. Grillet, Mid-infrared octave spanning supercontinuum generation to 8.5 μm in silicon-germanium waveguides, Optica 5 (2018) 360-366. https://doi.org/10.1364/OPTICA.5.000360.
[38] B. X. Xiang, Y. J. Ma, H. P. Han, M. Wang, H. Zhang, S. C. Ruan, Ultraviolet to near-infrared supercontinuum generation in a yttrium orthosilicate channel waveguide formed by ion implantation, Opt. Mater. Express 7 (2017) 1794-1803. https://doi.org/10.1364/OME.7.001794.
[39] A. Villeneuve, C. C. Yang, G. I. Stegeman, C. H. Lin, H. H. Lin, Nonlinear refractive-index and two-photon-absorption near half the band gap in AlGaAs, Appl. Phys. Lett. 62 (1993) 2465-2468. https://doi.org/10.1063/1.109320.
[40] O. K. Kim, W. G. Spitzer, Infrared reflectivity spectra and Raman spectra of Ga1-xAlxAs mixed crystals, J. Appl. Phys. 50 (1979) 4362-4370. https://doi.org/10.1063/1.326422.
[41] F. Leo, S. P. Gorza, S. Coen, B. Kuyken, G. Roelkens, Coherent supercontinuum generation in a silicon photonic wire in the telecommunication wavelength range, Opt. Lett. 40 (2015) 123-126. https://doi.org/10.1364/OL.40.000123.
[42] J. T. Lai, J. H. Yuan, Y. J. Cheng, C. Mei, X. Zhou, Q. Wu, B. B. Yan, K. R. Wang, K. P. Long, C. X. Yu, X. Z. Sang, Dispersion-engineered T-type germanium waveguide for mid-infrared supercontinuum and frequency comb generations in all-normal dispersion region, OSA Continuum 3 (2020) 2320-2331. https://doi.org/10.1364/OSAC.399941.
[43] Y. C. Zhang, H. J. Liu, Q. B. Sun, N. Huang, Z. L. Wang, Supercontinuum generation in strip/slot hybrid waveguide with flat and low dispersion, Appl. Opt. 54 (2015) 4850-4856. https://doi.org/10.1364/AO.54.004850.
[44] C. D. Li, P. P. Guo, W. Huang, W. Zhang, P. P. Xu, and P. Q. Zhang, Reverse-strip-structure Ge28Sb12Se60 chalcogenide glass waveguides prepared by micro-trench filling and lift-off, J. Opt. Soc. Am. B 37 (2020) 82-87. https://doi.org/10.1364/JOSAB.37.000082.